Full Length Article

# Three-dimensional grain growth during multi-layer printing of a nickel-based alloy Inconel 718

H.L. Wei[a], G.L. Knapp[b], T. Mukherjee[b], T. DebRoy[b],*

[a] School of Mechanical Engineering, Nanjing University of Science and Technology, Nanjing, 210094, China
[b] Department of Materials Science and Engineering, The Pennsylvania State University, University Park, PA, 16802, USA

## ARTICLE INFO

## ABSTRACT

Heterogeneous grain structure is a source of the inhomogeneity in structure and properties of the metallic components made by multi-layer additive manufacturing (AM). During AM, repeated heating and cooling during multi-layer deposition, local temperature gradient and solidification growth rate, deposit geometry, and molten pool shape and size govern the evolution of the grain structure. Here the effects of these causative factors on the heterogeneous grain growth during multi-layer laser deposition of Inconel 718 are examined by a Monte Carlo method based grain growth model. It is found that epitaxial columnar grain growth occurs from the substrate or previously deposited layer to the curved top surface of the deposit. The growth direction of these columnar grains is controlled by the molten pool shape and size. The grains in the previously deposited layers continue to grow because of the repeated heating and cooling during the deposition of the successive layers. Average longitudinal grain area decreases by approximately 80% when moving from the center to the edge of the deposit due to variable growth directions dependent on the local curvatures of the moving molten pool. The average horizontal grain area increases with the distance from the substrate, with a 20% increase in the horizontal grain area in a short distance from the third to the eighth layer, due to competitive solid-state grain growth causes increased grain size in previous layers.

## 1. Introduction

Inhomogeneity in microstructure and mechanical properties of laser-assisted directed energy deposition (DED-L) additive manufacturing (AM) components are affected by the spatial distribution of the grain structure [1–5]. Four unique attributes of the AM process result in heterogeneous grain growth in AM components. First, the evolution of the grain structure and solidification morphology depend on the shape and size of the moving molten pool [6,7]. Convective flow of liquid metal due to surface tension gradients on the top surface of the molten pool often controls the pool geometry. Ignoring the effects of molten metal convection may result in inaccurate pool geometry and unreliable grain structure and solidification morphology. Second, already deposited layers experience repeated heating and cooling during the deposition of successive layers [8]. These repeated temperature variations affect the grain structure due to both partial melting of the previous layer and growth of the grain structure in the solid state [9]. Third, in DED-L, alloy powders are melted by a laser beam and deposited on the top of a substrate or previously deposited layer. Therefore, the top surface of the deposited layer is often in a curved shape.

The shape and size of this curved top surface affect the direction of the grain growth [10]. Finally, local temperature gradient and solidification growth rate determine the solidification morphology and direction of maximum heat flow from the molten pool to the substrate, along which columnar grains tend to grow [11,12]. Both the local temperature gradient and the solidification growth rate depend on the specific location within a part, as spatial variation of these parameters can occur in different hatches and layers of the deposit. Therefore, effects of these simultaneously occurring physical processes on grain growth need to be considered in order to understand the causes of inhomogeneity in microstructure and properties of AM components.

In order to develop a comprehensive understanding of the role of the aforementioned causative factors, a combination of both experimental and theoretical approaches is needed. Since AM is a highly transient process, it is difficult to accurately capture the temporal evolution of grain growth by experiments alone. In addition, experimental understanding of the spatial distribution of grain structure in three-dimensions requires serial sectioning of the component at multiple planes. This approach is time consuming and often leads to confusing results. For example, columnar grains may appear to have

---

equiaxed morphologies at the plane sectioned perpendicular to their growth direction. A recourse is to develop, test and utilize a three-dimensional grain growth model of AM process. Several attempts have been made to model grain growth in AM. However, many existing grain growth models are in 2D [13,14] that are unable to provide the spatial distribution of grain structure and solidification morphologies for the entire three-dimensional component. Often predictions of grain growth are done for a single layer deposit [7,15]. These models do not take into account the repeated heating and cooling on the grain growth in a multi-layer deposit, and cannot take into account epitaxial growth from previous layers as reported in the literature [16–18]. Molten pool shape and size are often considered to be unchanged during the deposition process [19]. These models fail to include the effect of heat accumulation on the grain growth in a multi-layer deposit. Convective flow of molten metal often dominates the mechanism of heat transfer in the molten pool and thus governs the pool geometry. Calculated grain structure and solidification morphologies using models that ignore the liquid metal flow do not incorporate the influence of convective heat transfer in microstructure development [13,20–22]. Calculated grain structure and solidification morphologies using these models [13,20–22] often do not agree well with the experiments. Grain growth models often use simplified geometries to represent the deposited material in order to reduce complexity and computation costs [13,20–22]. Note that the curved surface of DED deposits [15,23] can impose significant constraint on the grain growth process. Some models neglect spatial variations in temperature gradients and solidification front velocities while coupling the grain growth model with heat transfer calculations [19,24]. In this work a mathematical framework is developed to reveal the effects of transient temperature field, molten pool and deposit geometries, repeated heating and cooling, temperature gradient and solidification growth rate on 3D spatial distribution and temporal evolution of grain growth in DED-L.

Here we examine the temporal evolution and spatial distribution of grain structure during multi-layer DED-L of Inconel alloy 718 (IN 718). The three-dimensional transient temperature field, molten pool and deposit geometries, and local values of temperature gradient and solidification growth rate are essential for grain growth calculations. These parameters are estimated using a well-tested heat transfer and fluid flow model of DED-L [23], and then grain structures are calculated using a three-dimensional Monte Carlo (MC) based method. The metallurgical variables calculated from the heat transfer and fluid flow model serve as critical input to the grain growth model. The calculated grain structures are compared with independent experimental results. Furthermore, the model is utilized to examine the roles of continuously moving pool and repeated heating and cooling during multi-layer deposition on temporal variation, spatial distribution and spatial inhomogeneity of grain size and topology.

## 2. Methodology

The role of the causative factors on the evolution of the 3D grain structure and solidification morphology are examined in two steps. First, a well-tested heat transfer and fluid flow model of DED-L is used to calculate three-dimensional transient temperature fields, molten pool dimensions, local temperature gradients and solidification growth rates. Second, based on the calculated results of the heat transfer and fluid flow model, grain structure and solidification morphology are estimated using a grain growth model. The grain growth model also calculates grain structure and solidification morphology in two steps. First, the solidification morphology is predicted based on the calculated temperature gradient and solidification growth rate [2]. Second, grain growth in the already solidified layers due to repeated heating and cooling during multi-layer deposition is estimated using a MC method based grain growth model. The methodology is explained in the following subsections.

### 2.1. Assumptions

Several simplified assumptions are made in the heat transfer and fluid flow simulation and the grain growth simulation to make the calculations tractable.

(1) The liquid metal flow is assumed to be incompressible and Newtonian. The effect of turbulence in the molten pool on heat transfer is considered by using enhanced thermal conductivity and viscosity of the liquid metal [25].

(2) The loss of alloying elements due to vaporization [1,8] and its effects on both heat loss and composition change are not considered in the calculations. The heat loss due to vaporization is estimated to be small compared to the heat input from the laser beam.

(3) Subgrain microstructure such as cells and dendrites are not considered. The proposed grain growth model focuses on the temporal and spatial variation of the structure on the scale of grains.

(4) Epitaxial growth of grains from the partially melted existing grains is assumed. The grain growth direction is determined by the local maximum heat flow direction. The grain growth rate depends on the local position at the solidification front of the molten pool [7].

(5) The solidification front is determined by the solidus isotherm [6]. The influence of undercooling on the deviation of the solidification front are not considered for simplicity [1,26].

(6) The formation of precipitates and their effects on grain growth are not considered for simplicity.

### 2.2. Estimation of 3D transient temperature fields and molten pool geometries

Three dimensional, transient temperature fields and molten pool and deposit geometries during DED-L of IN 718 are calculated through a well-tested 3D heat transfer and fluid model. The model solves conservation equations of mass, momentum and energy in three dimension to calculate the temperature and velocity fields, molten pool dimensions and multiple thermal cycles during the multi-layer deposition process. These equations are described in detail in our previous papers [2,23,27–30], and the salient features of the model are presented in Appendix A.1. Local temperature gradients and growth rates of the solidification front are calculated based on the transient three-dimensional temperature fields. The data [15,31,32] of the process parameters and the thermophysical properties of IN 718 used for the calculation are presented in Table 1. The data [31,33,34] used to calculate the surface tension and the temperature coefficient of the surface tension are presented in Table 2.

**Table 1**
Process parameters and thermophysical properties for the heat transfer and fluid flow modeling of DED-L of IN 718 [15,31,32].

| Variables | Value |
| --- | --- |
| Laser power (W) | 840 |
| Laser scanning speed (mm s$^{-1}$) | 10 |
| Laser beam radius (mm) | 1.1 |
| Layer thickness (mm) | 0.45 |
| Solidus temperature (K) | 1533 |
| Liquidus temperature (K) | 1609 |
| Density (kg m$^{-3}$) | 8100 |
| Thermal conductivity of solid (W m$^{-1}$ K$^{-1}$) | $0.56 + 2.9 \times 10^{-2}$ T $- 7 \times 10^{-6}$ T$^2$ |
| Specific heat of solid (J kg$^{-1}$ K$^{-1}$) | $360.4 + 0.026$ T $- 4 \times 10^{-6}$ T$^2$ |
| Viscosity of liquid (kg m$^{-1}$ s$^{-1}$) | $5 \times 10^{-3}$ |
| Latent heat of fusion (J kg$^{-1}$) | $2.1 \times 10^{5}$ |
| Coefficient of thermal expansion (K$^{-1}$) | $4.8 \times 10^{-5}$ |

**Table 2**
Data used for the calculation of surface tension and its temperature coefficient [31,33,34].

| Variables | Value |
|---|---|
| Surface tension at melting point, $\gamma_m$ (N m$^{-1}$) | 1.842 |
| d$\gamma$/d$T$ at melting point, $A$ (N m$^{-1}$ K$^{-1}$) | $-0.11$ |
| Surface excess of sulfur at saturation, $\Gamma_s$ (mol m$^{-2}$) | $1.3 \times 10^{-5}$ |
| Enthalpy of segregation, $\Delta H°$ (J kg$^{-1}$ mol$^{-1}$) | $-1.66 \times 10^5$ |
| Entropy factor, $k_1$ | $3.18 \times 10^{-3}$ |
| Gas constant, $R$ (J K$^{-1}$ mol$^{-1}$) | 8.314 |

**Table 3**
Data used in the grain growth model for MC simulation [9,34,43–45].

| Variables | Value |
|---|---|
| Initial grid spacing, $\lambda$ (μm) | 12 |
| Grain boundary energy, $\gamma$ (J m$^{-2}$) | 0.87 |
| Accommodation probability, $A$ | 1.0 |
| Average number per unit area at grain boundary, $Z$ (atoms m$^{-2}$) | $1.1 \times 10^{19}$ |
| Activation enthalpy for grain growth, $Q$ (J mol$^{-1}$) | $2.85 \times 10^5$ |
| Atomic molar volume, $V_m$ (m$^3$ mol$^{-1}$) | $7.2 \times 10^{-4}$ |
| Avagadro's number, $N_a$ (mol$^{-1}$) | $6.02 \times 10^{23}$ |
| Planck's constant, $h$ (J s) | $6.624 \times 10^{-34}$ |
| Activation entropy, $\Delta S_a$ (J mol$^{-1}$ K$^{-1}$) | 10.7 |

### 2.3. Calculation of the solidification morphology

A molten pool is generated under the irradiation of the laser beam and the liquid metal solidifies at the trailing edge of the molten pool during the cooling process of DED-L. The growth direction and the growth rate of the solidifying columnar grains are dependent on the characteristics of the molten pool which include the shape, size, and moving speed. Columnar grains tend to grow epitaxially from the partially melted grains in previous layers during the deposition of the subsequent layers. Thus, prediction of the size and shape of the molten pool are critical to the grain structure examination. In this work, the temperature field data of the computed molten pool from the aforementioned heat transfer and fluid flow model are imported to the grain growth model to simulate the grain structure in multi-layer DED-L of IN 718. The methodologies for the calculation of the heat flow direction and solidification rate at the solidification front of the molten pool are presented in Appendix A.2. The grain structure developed during solidification experiences further growth in the solid deposit.

### 2.4. Grain growth calculations in the already deposited layers

Multiple thermal cycles are experienced by a location in the deposit during the multi-layer DED-L process [35,36]. Migration of grain boundaries occurs in the solid region experiencing repetitive heating and cooling processes. The grain growth process in the solid deposit is simulated through the MC method [6,7,37–41] which originates from Pott's model [42]. The details of the algorithm and the application of the MC method can be found in literature [6,7,37–41] and the salient features relevant to the specific aspects of this work are presented in Appendix A.3.

Repetitive re-heating and re-melting of the solid metal below the depositing layer occurs, followed by the subsequent epitaxial growth of the grains in the solidifying deposit during the multi-layer DED-L process. Substantially elongated columnar grains are often generated which propagate through multiple layers. Meanwhile, there are grains produced and confined within the local layers and exhibit periodical features due to the layer-by-layer process of DED-L. The interdependent growth behavior of grains in the solidifying layers and the previously deposited layers are modeled considering the characteristics of the molten pool and the multiple thermal cycles as described above. The data used for the calculation are presented in Table 3 [9,34,43–45].

### 2.5. Computation procedures

Cartesian coordinates are used in the models developed in this work, as illustrated in Fig. 1. Unidirectional laser scanning directions along positive x-axis are applied for the multi-layer deposition. The build direction of multiple layers follows the positive z-coordinate. The layer width direction from its centerline follows the positive y-coordinate. Thus, the XY-plane represents the horizontal plane, the XZ-plane represents the longitudinal plane, and the YZ-plane represents the transverse plane.

The following procedures are carried out to complete the modeling of the heat transfer, liquid metal flow, and grain growth processes for
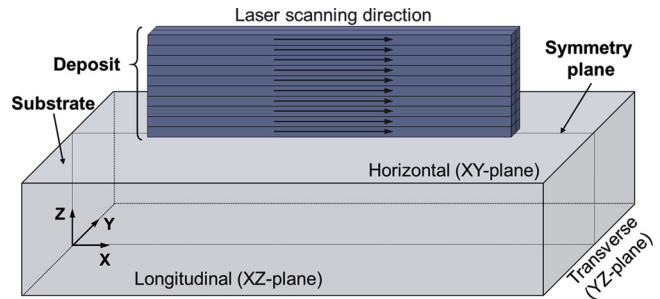


**Fig. 1.** Schematic view of the computational domain for the 3D model.

multi-layer DED-L of IN 718.

(1) The temperature and velocity fields, thermal cycles, and solidification parameters are calculated through the heat transfer and fluid flow model for multi-layer deposit.
(2) The temperature fields are interpolated from the heat transfer and fluid flow model to the grain growth model utilizing linear interpolation technique.
(3) The temperature field progresses one step ahead and the growth directions and growth rates of the columnar grains at the trailing edge of the molten pool are calculated.
(4) In the solidifying layer, columnar grains near the trailing edge of the molten pool grow epitaxially from the partially melted grains in the substrate or previously deposited layers.
(5) Grains in the solid region evolve due to the locally experienced thermal cycles, which affects the epitaxial growth of columnar grains during solidification.
(6) Steps (2) to (5) are repeated until the multi-layer deposition process has been completed.

## 3. Results and discussion

### 3.1. Effects of molten pool and deposit geometries on grain growth

#### 3.1.1. Estimation of molten pool and deposit geometries

The width, length, depth, and profile of the fusion zone define the geometry of the pool that develops during deposition of material. These variables depend on the conductive heat transfer to the surrounding substrate and on the distribution of heat due to surface-tension driven fluid flow within the fusion zone. Fig. 2 shows the three-dimensional temperature and velocity fields when the laser beam is at the mid length of the track during the deposition of the first layer. The red region bounded by the liquidus temperature isotherm (1609 K) represents the liquid region of the molten pool. The liquidus and solidus (1533 K) temperature isotherms bound the two-phase region of the molten pool, also called the mushy zone. Isotherms are compressed near the leading edge and expanded near the trailing edge of the molten pool due to scanning along the positive x-direction. In DED-L, the deposit is made
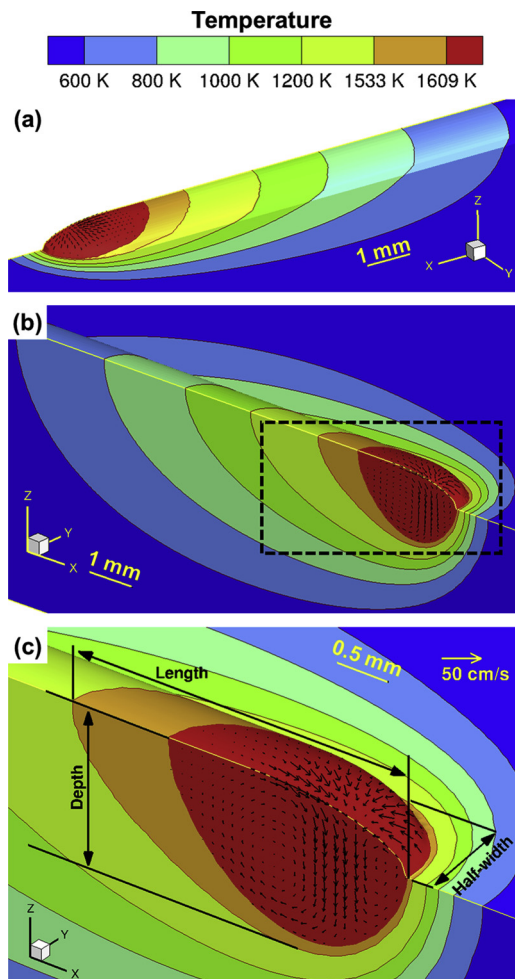
**Fig. 2.** Three-dimensional temperature and velocity fields during the first layer of DED-L of IN 718. Laser power: 840 W, scanning speed: 10 mm/s. (a) and (b) show the views from the two sides of the deposit. (c) is the magnified view of the boxed region in figure (b) near the molten pool. Scale bars are for the x-axis. The scanning direction is along the positive x-axis.

by melting and accumulating powder particles. Therefore, the top surface of the deposit is curved, with the height at a maximum at the center and decreasing along the y-direction away from the center of the deposit, as shown in Figs. 2(a–b).

Fig. 2(c) provides a closer view of the molten pool and shows the measurements used to define the molten pool geometry. Black velocity vectors represent the convective flow of the liquid metal driven by the surface tension gradient on the top surface. The magnitude of these velocities can be estimated by comparing their length with that of the reference vector provided in Fig. 2(c). The flow velocity of the liquid metal is on the order of 300 mm/s, which indicates that convective heat transfer dominates the transport of energy within the molten pool. For most alloys, the liquid metal flows from the center to the periphery of the molten pool. However, the grade of IN 718 considered here has a 0.015 wt.% sulfur that acts as a surface active element [15] resulting in a positive surface tension gradient (d$\gamma$/dT). This results in a convective flow from the periphery to the center of the molten pool, as shown in Fig. 2. Inward flow of the liquid metal enhances the heat transfer along z-direction from the heat source, leading to a deep molten pool [46–48].

### 3.1.2. Evolution of grain structure depending on moving pool

The temporal variations of the molten pool dimensions are shown in Fig. 3. As the deposition of a particular layer progresses, more heat
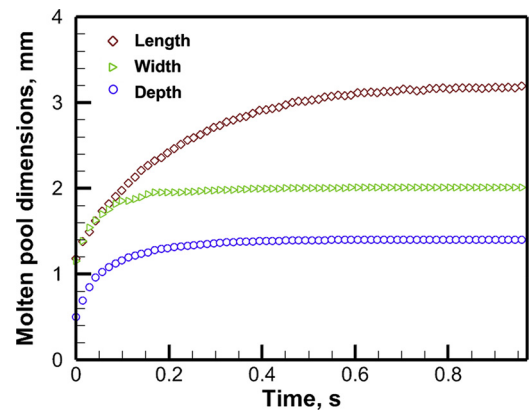


**Fig. 3.** Variation of the molten pool dimensions with time during the first layer for DED-L of IN 718. Laser power: 840 W, scanning speed: 10 mm/s.

accumulates in the build. That results in a continuous expansion of the molten pool with time until a quasi-steady state is reached. In quasi-steady state, the molten pool itself does not change over time, but the temperature fields away from the pool are not necessarily constant. For example, Fig. 3 shows that for the 1st layer the length, depth and width of the molten pool reach quasi-steady state in around 0.8, 0.3 and 0.3 s, respectively. It is evident from Fig. 3 that during the deposition of a particular layer, the quasi-steady state is reached within a short time. Quasi-steady state means that the local temperature gradient, G, and the solidification rate, R, will effectively be constant for a given location on the molten pool. Therefore, the quasi-steady state pool dimensions can be used throughout the deposition process for predicting overall grain growth, supporting the approach taken by Rodgers et al. [19]. However, it is noted that the time taken to reach quasi-steady state will vary if the material and/or the processing parameters are changed [49].

Both G and R vary spatially [7,50], so local values are calculated using the heat transfer and fluid flow model to predict the solidification morphologies. For example, at the mid-length of the first layer at the centerline of the trailing edge of the molten pool on the top surface the values of G and R are 92 K/mm and 10 mm/s, respectively. These values of G and R indicate that the grain morphology of that layer is columnar, based on the literature [51–53], so grains will tend to solidify by epitaxial growth on the previously solidified grains. The G and R values for the entire layer never reaches the value that indicates columnar equiaxed transition (CET) for Inconel 718 [52,54]. The direction of grain growth also depends on the local values of G. For example, columnar grains grow along the maximum heat flow direction determined by the local values of the temperature gradient (G). In DED-L, the direction of maximum heat flow from the molten pool is perpendicular to the boundary of the molten pool at the trailing edge [2]. Fig. 4 schematically shows that the growth direction of the columnar grains are always perpendicular to the trailing edge of the molten pool. For a
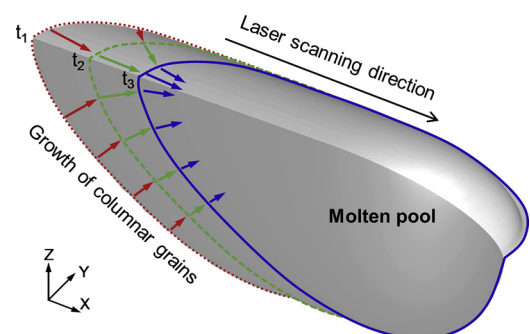


**Fig. 4.** Schematic illustration of the progress of the columnar grain growth based on the moving molten pool.
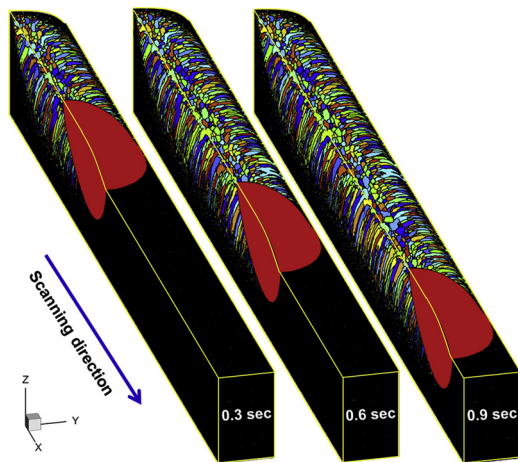
**Fig. 5.** Evolution of the grain structure visualized in the longitudinal section and the curved top surface of the sample during single layer DED-L of IN 718. laser power: 840 W, scanning speed: 10 mm/s.

continuously moving molten pool in DED-L, the maximum heat flow direction changes as the pool progresses. Therefore, the columnar grains bend towards the scanning direction as shown in Fig. 4.

This phenomenon can be seen in Fig. 5, which shows the development of the grain structure in three-dimensions as the molten pool progresses during the first layer deposition. Grains are visualized with coloring based on the arbitrary index number of the grain. The columnar grains produced during solidification grow epitaxially from the partially melted equiaxed grains in the substrate. These long, columnar grains bend and follow the trailing edge of the molten pool. The evolution of the grain structure presented in Fig. 5 indicates that the solidification process is constricted by the geometry of the moving localized molten pool. Causative factors for heat transfer and fluid flow within the molten pool further affect the profile of the molten pool [33,47]. Therefore, the resultant variable solidification conditions influence the temporal evolution and spatial distribution of the grain structure.

### 3.1.3. Effects of pool and deposit shapes on grain structure

Fig. 6 shows that the calculated grain structure agrees well with the experimental observation [15] in the transverse section of a single layer sample of IN 718 deposited by DED-L. Both experimental and calculated results show that the columnar grains grow from the fusion zone
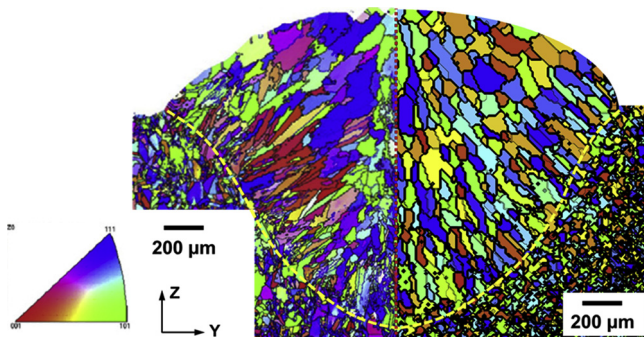


**Fig. 6.** Comparison of the experimental (left) and calculated (right) results for grain structure observed in the transverse section (YZ plane) for single layer DED-L of IN 718. Laser power: 840 W, scanning speed: 10 mm/s. The experimental result was adapted from the literature [15]. Fusion zone boundary is marked by the yellow dashed lines. The various colors in the simulated results represents the index numbers of different grains. (For interpretation of the references to colour in this figure legend, the reader is referred to the web version of this article).

boundary towards the curved top surface of the deposit. The grain growth angle predicted by the model agrees reasonably well with the experiment. Fine grains near the molten pool boundary and coarse grains near the upper center part are observed. Near the boundary of the pool, where the pool is nearly orthogonal to the observed cross-section, the grain growth direction is approximately in plane with the transverse section, because columnar grain growth occurs perpendicular to the molten pool boundary. In the other regions of the sample, grain growth is out-of-plane, such that the full length of the columnar grains is not observable. Calculated grain structures in the horizontal and longitudinal sectional planes are further compared with corresponding experimental observations in Fig. 7. The morphologies, sizes and growth directions of the grains match well between the simulated and experimentally characterized results, which demonstrate the validity of the 3D grain growth model developed in this study. A possible source for the differences between the experimental and modeling results is the assumption that the grain growth direction is the same as the maximum heat flow directions at all locations on the molten pool boundary. This assumption provides computational efficiency although the growth is a result of the competition between the maximum heat flow directions and the easy growth directions. Comparison of grain morphologies in multiple planes is necessary, due to the 3D geometry of the molten pool. The elongated shape of the grains in Fig. 6 is not visible in Fig. 7, due the grains being oriented nearly perpendicular to the viewing planes.

### 3.2. Effect of repeated heating and cooling during multi-layer deposition

The aforementioned mechanisms of the grain growth for a particular layer repeats itself for multi-layer deposition. However, in a multi-layer deposit the already deposited layers experience repeated heating and cooling during the deposition of the upper layers. This results in either re-melting or coarsening of grains in the already deposited layers, depending on if the heating is sufficient to melt the previously deposited material. Therefore, the molten pool geometry is not the only mechanism that influences grain sizes and shapes, because the thermal history of the location also changes grain structure.

Fig. 8 shows the temporal evolution of the grain structure during 10 layers of DED-L of IN 718. The 2nd, 6th, and 10th layers serve as examples to demonstrate the variation of the grains with the progress of the build. Partially melted grains at the trailing edge of the molten pool serve as nuclei for the epitaxial growth of the columnar grains during solidification. During the deposition of a particular layer, the layer below is partially re-melted and re-solidified. For example, first layer is re-melted during the deposition of the second layer as shown in Fig. 8. This re-melting eliminates much of the curvature in the grain growth caused by the curved surface of the deposit. The curvature seen in the grains during the deposition of the second layer disappears by the time the sixth layer is deposited, and the grains are long, straight columnar grains angled normal to the lower portion of the molten pool.

Reheating and cooling of a particular layer can be understood by calculating the variation of temperature with time for a particular location of that layer. Fig. 9 shows the transient temperature variations for four locations at the fourth layer while depositing fourth to eighth layers. The locations A, B and C experience melting during the deposition of the fourth layer. In addition, location A experiences re-melting during the depositions of both fifth and sixth layers and location B undergoes re-melting only during the deposition of fifth layer. In contrast, monitoring locations C and D do not experience re-melting during the depositions of subsequent layers. However, these two locations undergo multiple reheating and cooling in solid state. These reheating and cooling affect the temporal evolution of the grains and their sizes. Fig. 10 shows the variations of the grain structure on a horizontal plane that contains the location A, marked by a white circle, while depositing the fourth through eighth layers. Fig. 10 (a) shows the grain structure during the deposition of the fourth layer. The grains in this
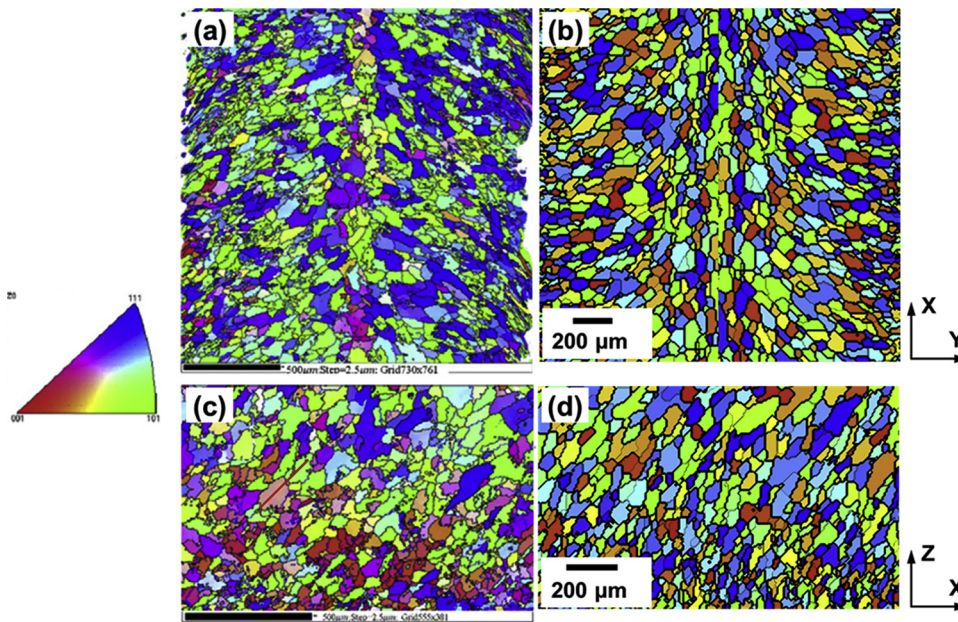
**Fig. 7.** Comparison of the experimental and calculated results for grain structure observed in (a) and (b) horizontal sections (XY plane), (c) and (d) longitudinal sections (XZ plane) for single layer DED-L of IN 718. (a) and (c): EBSD results taken from the literature [15], (b) and (d): simulation results. Laser power: 840 W, scanning speed: 10 mm/s. The various colors in the simulated results represents the index numbers of different grains.
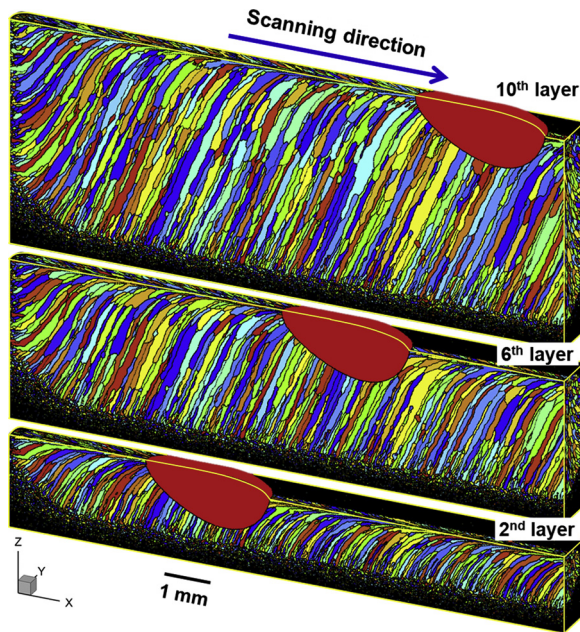


**Fig. 8.** Temporal evolution of the grain structure visualized in the longitudinal central plane and the top surface of the deposit for ten layers DED-L of IN 718. Laser power: 840 W, scanning speed: 10 mm/s.



**Fig. 9.** Thermal cycles experienced at four monitoring locations, A–D, during the deposition of the fourth to the eighth layers. The location A is 0.2 mm away from the top of the fourth layer. The distance between the neighboring monitoring locations is 0.45 mm.

sectional plane experience re-melting during the deposition of the fifth and sixth layers, with the morphologies of the grains reformed during re-solidification, as shown in Fig. 10 (b–c). During the depositions of the seventh through eighth layers, the grains in this selected sectional plane experience solid-state growth due to the repeated heating and cooling, as shown in Fig. 10 (d–e). However, during the deposition of the eighth layer, the solid-state growth is insignificant because of relatively low reheating temperature as shown in Fig. 9. Though this phenomenon is only highlighted in one region, solid-state grain growth occurs throughout the previously deposited layers when reheating temperatures are high enough. Grains compete as they grow in the solid metal via boundary migration driven by the reduction of total grain boundary energy [9]. The grain structure formed during solidification acts as the initial condition and thus affect the subsequent grain grow in the solid metal. In this way, the geometry of the molten pool that
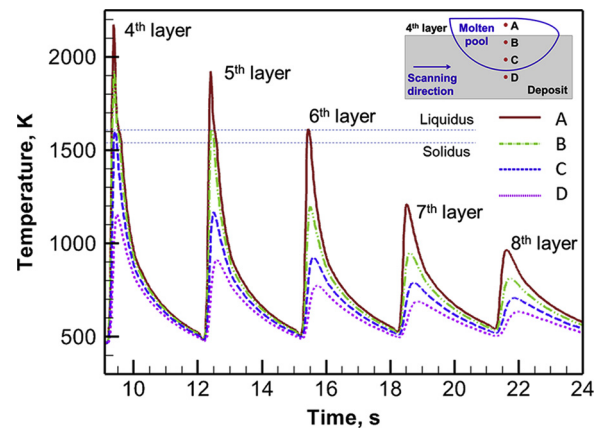
determines the initial solidification structure and the solid-state grain growth are intricately linked.

### 3.3. Spatial inhomogeneity in the grain structure of a multi-layer deposit

The spatial variations of temperature gradient and solidification growth rate and the thermal cycles during multi-layer deposition result in spatial inhomogeneity in the grain structure. Fig. 11 shows the spatial distribution of the grain structure in a series of longitudinal planes. The morphologies and dimensions of the grains appear significantly different in these planes. In the central plane shown in Fig. 11 (a), elongated columnar grains propagating through multiple layers are present. Moreover, it can be observed that these columnar grains are inclined to the slope of the molten pool's trailing edge. The inclination angles of the columnar grains with the horizontal plane are about 60° through the build height. The origin of the growth directions of these columnar grains is from the solidification process constricted by the moving molten pool. The local maximum heat flow directions at the trailing edge of the molten pool are 0° on the top and 90° at the bottom of the molten pool. The maximum heat flow direction is about 60° for the major part through the depth of the molten pool. The growth
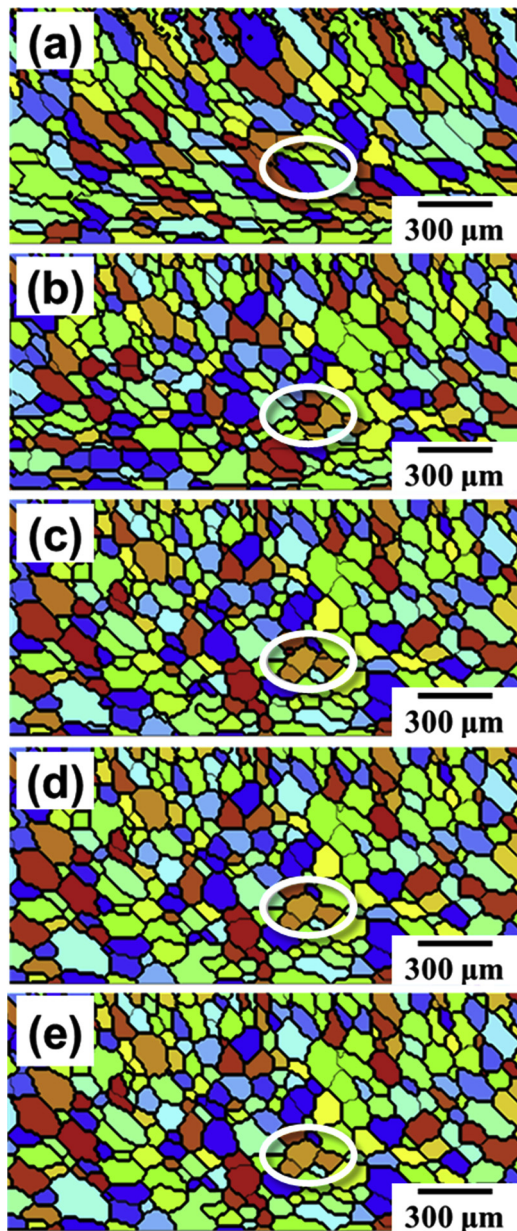
**Fig. 10.** Monitored grain structure in a selected horizontal sectional plane (XY) containing location A (Fig. 9) after the deposition of the (a) fourth layer, (b) fifth layer, (c) sixth layer, and (d) seventh layer, (e) eighth layer. Location A is marked with a white circle in all subfigures.

direction of a columnar grain varies dynamically with respect to its local position at the trailing edge of the molten pool during the solidification process.

The dynamic directional growth of the columnar grains appears in the upper most region of Fig. 11 (a). However, as discussed earlier, the curvature of the grains disappears as each layer is re-melted. The microstructure is predominantly composed of columnar grains with inclination angle of about 60° except in the uppermost region near the top of the deposit. The unidirectional scanning direction of the laser beam generates a quasi-steady state molten pool approximately 0.5 s after the start of scanning in each layer, so the temperature gradient direction remains constant throughout the build and allows epitaxial growth seen in Fig. 11 (a) to occur. Fig. 11(b)–(d) show the longitudinal sectional planes with distances of 60 μm, 240 μm, and 840 μm from the longitudinal central plane, respectively. It can be observed that the grains appear less elongated as the distance from the central longitudinal

plane is increased. Moreover, the average area of the grains decreases with larger distance from the longitudinal central plane. However, the curvature of the molten pool is such that moving away from the central plane, the grain growth direction is increasingly more perpendicular to the longitudinal plane. The influence of the y-direction component on the maximum heat flow directions increases with larger distances from the central longitudinal plane, which correspondingly affects the growth directions of the columnar grains. While the general grain morphology is similar, i.e., columnar, heterogeneity in the planar cross-sections occurs due to variations in the local growth directions of the grains.

Fig. 12 shows the variation of the grain structure in series of horizontal sections for a ten-layer build. Only the local sections of the columnar grains with near equiaxed appearances can be observed in the horizontal planes. Cross-sectional areas of the grains increase with greater distance from the bottom of the substrate However, unlike the longitudinal sections, the apparent shape of the grains remains similar throughout the height of the build. Pool geometry is nearly constant throughout the build, so there is no source for differences in the shape of the grains for horizontal planes near the top and bottom of the build. That said, increasing areas of the grains indicates that competitive growth is playing a role in eliminating smaller grains from the substrate and previous layers, meaning that epitaxial grow in higher layers occurs on larger grains.

Quantitative variation of the average grain area and aspect ratio is examined for series of longitudinal and horizontal sectional planes in Fig. 13 and Fig. 14. The aspect ratio is the ratio of the height over the width of a certain section of a grain, with height and width defined relative to the vertical and horizontal axes of the plane, respectively. The length and height of the selected longitudinal sectional planes are 4 mm and 3 mm, respectively. The bottom of the sectional plane coincides with the bottom of the third layer. Three sets of measurements are carried out in different regions along the laser scanning direction. The areas of the grains in corresponding sectional planes are averaged with the standard deviations displayed as the error bars shown in the figure. The length and width of the horizontal sectional planes are 4 mm and 1 mm, respectively. The increment distance between two neighboring longitudinal or horizontal sectional planes is 12 μm, which is the mesh size of the grain growth model. The selected sectional planes are schematically shown by the insets of Figs. 13 and 14.

Fig. 13(a) shows the average grain areas in the longitudinal sectional planes dropping by approximately 80% when moving from the center of the deposit to the edge. Fig. 14(a) supports the observation from Fig. 11 that the grain size change is largely due to the changing orientation of the columnar grains, because the aspect ratio approaches unity as the distance from the central plane increases. Equiaxed grains do not form with the calculated solidification conditions, so the change in apparent aspect ratio must be due to columnar grain orientation misalignment with the observed section.

In the horizontal sectional planes, the average grain area increases with the build height as shown in Fig. 13(b). Average area of the grains is overall much less than in the longitudinal sections due to the lack of observed columnar grains, but there is still a 20% increase in grain size over three millimeters of build height. Local variations of the grain areas result from the periodical solidification and partial re-melting of the deposited layers during the build process. In a single layer, the sectional areas of the columnar grains increase with large distance from the bottom of the layer mainly due to the heavier inclination of the grains. When a layer is partially re-melted and grains in the new layer continue to grow, the grain areas undergo the above variation once again. Variation of the aspect ratios of the grains in the horizontal planes is minimal, especially compared to the longitudinal planes. Fig. 14(b) shows the average aspect ratio of the grains remains close to 2.0, indicating only a slight elongation of the grains. The nearly constant aspect ratio suggests that grain area increases are due to actual increases in grain size, and that it is not due to grain orientation change
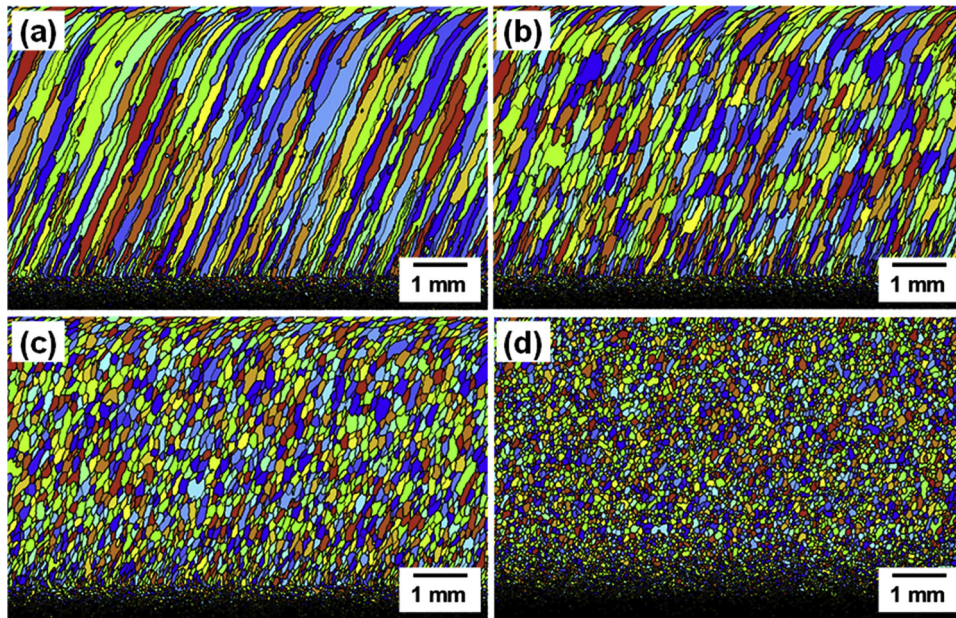
**Fig. 11.** Spatial variation of grain structure visualized in series of longitudinal sections (XZ planes) for 10 layers DED-L of IN 718. (a) - (d) are sectional planes with distances of 0.0 μm, 60 μm, 240 μm, and 840 μm from the longitudinal central plane (y = 0 μm), respectively.
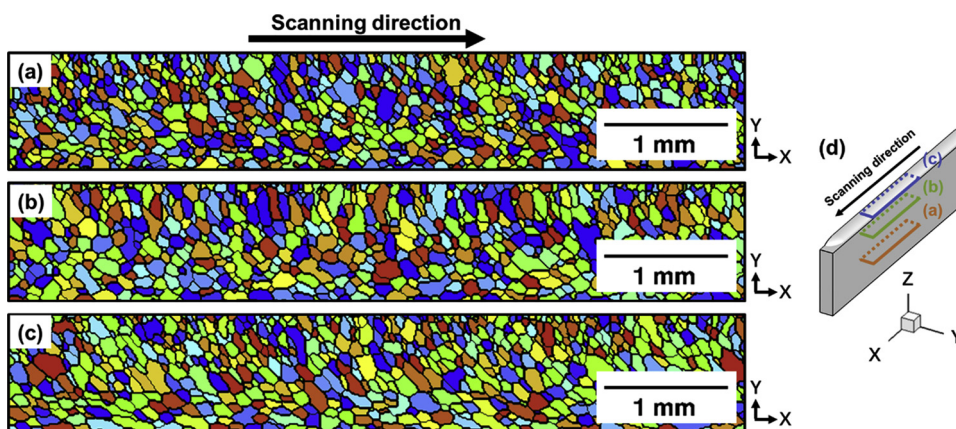


**Fig. 12.** Spatial variation of grain structure visualized in series of horizontal sectional planes constructed for 10 layers DED-L of IN 718. (a) 1.5 mm, (b) 3.5 mm, (c) 6.0 mm from the bottom of the substrate. (d) schematic showing the approximate locations of the horizontal planes within the part.

like in the longitudinal sections. This further supports earlier discussion suggesting that competitive grain growth causes the average grain size in the previously deposited layers to increase. Because of epitaxial growth, the size of solidified grains is largely dependent on the size of the previous layers' grains.

This heterogeneity has implications for both characterization of microstructure and mechanical properties. The strikingly different appearances of the columnar grains demonstrated in various sectional planes indicate that the selection of the 2D sectional planes for grain structure examination has significant influences on the characterization results. The 2D sections of the columnar grains shown in Fig. 11(c) can be misleading since the cross-sectional view of columnar grains may appear to have equiaxed morphologies. Even with electron backscatter diffraction to show the orientation of the grains, such as experimental results in Fig. 7(a) [15], it is not always clear from a single cross-section if grains are columnar grains oriented with a temperature gradient perpendicular to the viewing section or randomly oriented equiaxed grains. Consequently, assessment of the representative grain size for a part is difficult with only a single cross-section. If determining material strength from Hall-Petch type relationships, heterogeneity introduces a source of significant error. Variations in grain areas between the

horizontal and longitudinal planes seen in Fig. 13 may also lead to anisotropic material properties when loading in the horizontal and longitudinal planes.

In brief, the solidification process is influenced by the moving molten pool geometry, the curved surface of the deposit, re-melting and re-solidification of previous layers, and solid-state grain growth during multiple heating and cooling cycles. These factors produce the non-uniform, heterogeneous grain structure in AM. Furthermore, thorough examination of the grain structure through a single sectional plane can be a poor representation of the overall grain structure. The research presented in this work highlights the challenges faced by the experimental characterization of the 3D microstructure and provides insight about the grain structure due to a unidirectional laser scanning strategy.

## 4. Conclusions

The temporal evolution and spatial distribution of the three-dimensional grain structure and solidification morphology are elucidated during the multi-layer laser deposition of Inconel 718. Three-dimensional transient temperature fields, fusion zone geometries, and the
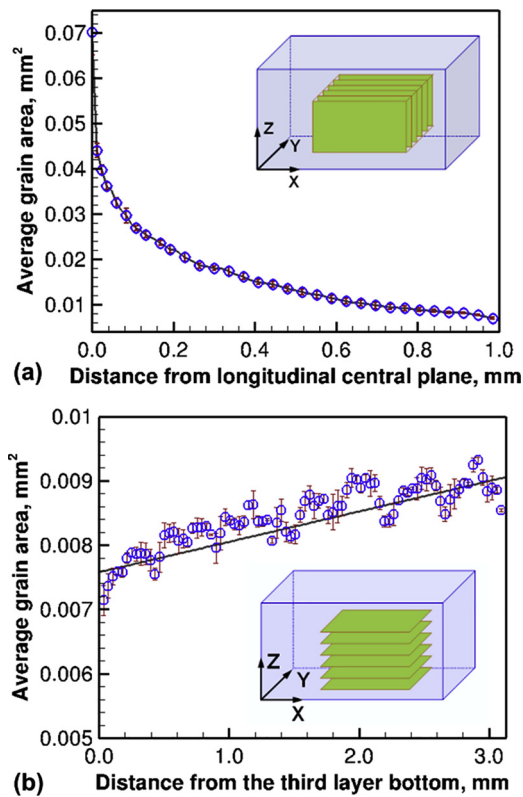
**Fig. 13.** Variation of the average grain areas in series sectional planes: (a) longitudinal planes with larger distances from the longitudinal central plane, (b) horizontal planes with larger distances from the bottom of the third layer.

local temperature gradient and solidification growth rate are estimated using a well-tested heat transfer and fluid flow model of DED-L. The computed results of grain structures in three orthogonal planes agreed well with the independent experimental data. Below are the specific findings.

(1) The continuous movement of the molten pool during the deposition of a particular layer facilitates the epitaxial growth of the columnar grains that follow the direction of maximum heat flow from the molten pool to the substrate. It has been found that the grains start growing perpendicular to the molten pool boundary and continue up to the curved top surface of the deposit.
(2) Repeated heating and cooling during the deposition of successive layers has significant effect on grain growth. For example, average grain size in lower layers was found to increase because of the re-melting of the layers and the subsequent epitaxial growth during solidification. Moreover, grains grow due to the repeated heating and cooling during the deposition of upper layers. However, after depositing four layers in the case of this work, the effect of heating and cooling in lower layers becomes insignificant and the grain size remains constant.
(3) The average longitudinal grain area decreases by approximately



**Fig. 14.** Variation of the average aspect ratios of the grains in series sectional planes: (a) longitudinal planes with larger distances from the longitudinal central plane, (b) horizontal planes with larger distances from the bottom of the third layer.

80% when moving from the center to the edge of the deposit. Such variation originates from the variable growth directions of the columnar grains that are dependent on the local curvatures of the moving molten pool.
(4) The average horizontal grain area is found to increase with distance from the substrate, with 20% increase in the horizontal grain area from the third to the eighth layer. Competitive solid-state grain growth causes increased grain size in previous layers. Epitaxial growth from previous layers means that as grain size of the previous layers increases, so too does the grain size of the current layer.

### Acknowledgements

### Appendix A. Transport process and grain growth model for DED-L of IN 718

*A.1. Heat transfer and fluid flow model for DED-L of IN 718*

In DED-L, the deposit is formed due to the accumulation of the molten material on the substrate or previously deposited layers. Therefore, the deposit takes a crown like shape with the height being tallest at the center and decreasing with the distance from the center. The shape and size of this curved deposit depend on the powder mass flow rate, scanning speed and the efficiency of the molten pool to catch depositing powder and are calculated based on the methodology proposed by Knapp et al [23].

The total heat energy supplied by the laser beam in DED-L process is absorbed in two steps [1]. First, a part of that energy is absorbed by the powders during their flight from the nozzle to the deposit. Second, the powders deposited on the build absorb heat and melt. The first part of the
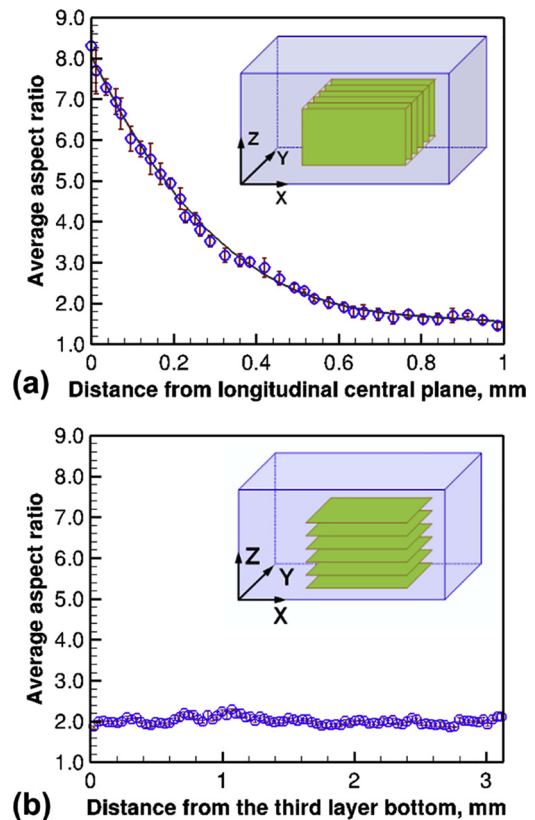
energy is considered using a volumetric heat source and the second part is modeled using a surface heat flux whose intensity varies in a Gaussian manner [23].

The boundary conditions for the energy conservation equation include convective and radiative heat losses from the surfaces of the deposit and substrate. With the progress of the deposition, the total surface area of the deposit increases and the boundary conditions are updated. Spatial variation in pool surface temperature creates a surface tension gradient that drives the convective flow of molten metal inside the pool. The temperature gradient along the 3D curved surface ($G$) has three components along the x-, y-, and z-directions ($G_x$, $G_y$, $G_z$, respectively). The Marangoni stress at any point on the curved surface along the x-, y-, and z-directions, respectively, is [27],

$$\tau_x = \mu \frac{d\,u}{d\,z} = \frac{d\,\gamma}{d\,T} G_x \tag{A.1}$$

$$\tau_y = \mu \frac{d\,v}{d\,z} = \frac{d\,\gamma}{d\,T} G_y \tag{A.2}$$

$$\tau_z = \mu \frac{d\,w}{d\,r} = \frac{d\,\gamma}{d\,T} G_z \tag{A.3}$$

where $T$ is the temperature, $\gamma$ is the surface tension, $\mu$ is the viscosity of the liquid metal, $r$ is the radial distance from the central axis of the heat source, and $u$, $v$, and $w$ are the velocities of the liquid metal along the x-, y-, and z-directions, respectively. The value of surface tension gradient with respect to temperature ($d\gamma/dT$) for most alloys without surface-active element is a negative constant [33,46,47]. However, for the IN 718 alloy considered here, sulfur acts as a surface-active element and consequently surface tension varies with temperature. It has been reported that the behavior of sulfur in IN 718 can be assumed to be similar to that in Fe-Cr-Ni alloys [34,55]. The local surface tension of the alloy, $\gamma$, in the liquid metal is calculated by [33,46,56,57]:

$$\gamma = \gamma_m - A[T - T_m] - RT\Gamma_s \ln[1 + K a_s] \tag{A.4}$$

$$K = k_1 \exp\left(\frac{\Delta H^\circ}{RT}\right) \tag{A.5}$$

The temperature coefficient of surface tension, $d\gamma/dT$, can be calculated by differentiating Eq. (A.4) with respect to $T$ [33,46]:

$$\frac{d\gamma}{dT} = -A - R\Gamma_s \ln[1 + KC] - \frac{KC}{1 + KC}\frac{\Gamma_s \Delta H^\circ}{T} \tag{A.6}$$

where $\gamma_m$ is the surface tension of the pure material at the melting point $T_m$, $A$ is the negative of the temperature coefficient of surface tension, $T$ is the local temperature of the molten metal, $R$ is the gas constant, $\Gamma_s$ is the surface access at saturation, $K$ is the adsorption coefficient, $k_1$ is a constant related to the entropy of segregation, $\Delta H^\circ$ is the standard heat of adsorption, and $a_s$ is the activity of sulfur which is its weight percent in the material.

### A.2. Calculation of maximum heat flow direction and solidification rate

For polycrystalline materials such as the IN 718 alloys studied in this work, the grain growth direction coincides with the local maximum heat flow direction at the trailing boundary of the molten pool. The direction of heat transfer at the local site of the molten pool boundary is normal to the isosurface and can be computed by [7]:

$$\nabla T = \frac{\partial T}{\partial x}i + \frac{\partial T}{\partial y}j + \frac{\partial T}{\partial z}k \tag{A.7}$$

where $T$ is the local temperature and $i$, $j$ and $k$ are unit vectors along the laser scanning, width, and build directions, respectively. The temperature gradient is the magnitude of $\nabla T$, which can be calculated as [58]:

$$G = \|\nabla T\| = \sqrt{\left(\frac{\partial T}{\partial x}\right)^2 + \left(\frac{\partial T}{\partial y}\right)^2 + \left(\frac{\partial T}{\partial z}\right)^2} \tag{A.8}$$

The local growth direction of a columnar grain varies with its actual position at the trailing edge of the molten pool according to Eq. (A.7). For example, a grain tends to grow along the vertical direction near the bottom of the molten pool in the longitudinal central plane due to the dominant heat flow along the z-direction. When the same grain progresses to the near surface region, it alters to grow near horizontally due to the dominant factor of the x-direction heat flow. These local heat flow directions are computed at each time-step during the moving process of the molten pool according to Eqs. (A.7) and (A.8). The growth directions of the columnar grains vary correspondingly with the maximum heat flow directions in the 3D computational domain for multi-layer deposition.

Apart from the variable local growth directions of the columnar grains, the local growth rates of the columnar grains change correspondingly during the solidification process. The angle, $\theta$, between the grain growth direction and the laser scanning direction is calculate by:

$$\cos\theta = \frac{-\partial T/\partial x}{G} \tag{A.9}$$

The local grain growth rate, $R$, can be calculated respect to the laser scanning speed, $v$, as:

$$R = v \cdot \cos\theta \tag{A.10}$$

Eqs. (A.9) and (A.10) indicate that the local growth rate of a columnar grain is zero at locations where the heat flow direction is perpendicular to the laser scanning direction. Thus, the zero values of $R$ appear at the dividing line separating the leading melting interface and trailing solidification interface of the molten pool respect to the solid metal. Moreover, the maximum value of $R$ appears at the trailing point of the solidification surface on the top surface where the heat flow direction is parallel with the laser scanning direction. Therefore, upon the initialization of a columnar grain starting at the dividing line for melting and solidification in the 3D domain, the local growth rate for that grain increases gradually as the

solidification progresses.

*A.3. Monte Carlo method to calculate grain growth in already deposited layers*

The migration of the grain boundaries in the solid deposit is simulated through MC technique. The grain boundary energy is represented by the interaction between nearest neighbor lattice sites, with unlike orientations resulting in higher total energy. The kinetics for the migration of grain boundaries are simulated by examining the variation of the system energy through randomly changing the orientation of a site to one of the orientations of its nearest neighbors. Initially all grids in the solid region are assigned a random integral number between one and $q$ representing the orientation. The value of $q$ is 48, which specifies the total number of possible grain orientations. The grids in the liquid region have an index of zero. The probability, $p$, to select a site depends on thermal cycles that the site experiences and can be calculated by [6,7,37]:

$$p = \frac{t_{MCS}}{t_{MCSMAX}} \tag{A.11}$$

where $t_{MCS}$ is the MC time for a local site and $t_{MCSMAX}$ is the maximum MC time for all the sites in the computation domain. Grain boundary migration model is used to calculate $t_{MCS}$ considering the thermal cycles and the material properties [6,7,37]:

$$t_{MCS} = \left\{ \frac{1}{K_1 \lambda} \left[ \frac{4\gamma A Z V_m^2}{N_a^2 h} e^{\Delta S_a/R} \sum_i \left( \Delta t_i \exp\left(-\frac{Q}{RT_i}\right) \right) + L_0^2 \right]^{\frac{1}{2}} - \frac{1}{K_1} \right\}^{\frac{1}{n_1}} \tag{A.12}$$

where $\lambda$ is the grid spacing, $K_1$ and $n_1$ are model constants, $\gamma$ is the grain boundary energy, $A$ is the accommodation probability, $Z$ is the average number of atoms per unit area at the grain boundary, $V_m$ is the atomic molar volume, $N_a$ is Avogadro's number, $h$ is Planck's constant, $\Delta S_a$ is the activation entropy, $Q$ is that activation enthalpy for grain growth, $T$ is temperature, $R$ is the gas constant, $L_0$ is the initial average grain size, and $t$ is time.

# References

[1] T. DebRoy, H.L. Wei, J.S. Zuback, T. Mukherjee, J.W. Elmer, J.O. Milewski, A.M. Beese, A. Wilson-Heid, A. De, W. Zhang, Additive manufacturing of metallic components – process, structure and properties, Prog. Mater. Sci. 92 (2018) 112–224.

[2] H.L. Wei, J. Mazumder, T. DebRoy, Evolution of solidification texture during additive manufacturing, Sci. Rep. 5 (2015) Article number: 16446.

[3] G.F. Sun, R. Zhou, J.Z. Lu, J. Mazumder, Evaluation of defect density, microstructure, residual stress, elastic modulus, hardness and strength of laser-deposited AISI 4340 steel, Acta Mater. 84 (2015) 172–189.

[4] D.D. Gu, W. Meiners, K. Wissenbach, R. Poprawe, Laser additive manufacturing of metallic components: materials, processes and mechanisms, Int. Mater. Rev. 57 (3) (2012) 133–164.

[5] W.J. Sames, F.A. List, S. Pannala, R.R. Dehoff, S.S. Babu, The metallurgy and processing science of metal additive manufacturing, Int. Mater. Rev. 61 (5) (2016) 315–360.

[6] H.L. Wei, J.W. Elmer, T. DebRoy, Crystal growth during keyhole mode laser welding, Acta Mater. 133 (2017) 10–20.

[7] H.L. Wei, J.W. Elmer, T. DebRoy, Three-dimensional modeling of grain structure evolution during welding of an aluminum alloy, Acta Mater. 126 (2017) 413–425.

[8] T. Mukherjee, J.S. Zuback, A. De, T. DebRoy, Printability of alloys for additive manufacturing, Sci. Rep. 6 (2016) Article number: 19717.

[9] S. Mishra, T. DebRoy, Non-isothermal grain growth in metals and alloys, Mater. Sci. Technol. 22 (3) (2006) 253–278.

[10] V. Ocelík, I. Furár, J.T.M. De Hosson, Microstructure and properties of laser clad coatings studied by orientation imaging microscopy, Acta Mater. 58 (20) (2010) 6763–6772.

[11] Y. Zhu, J. Li, X. Tian, H. Wang, D. Liu, Microstructure and mechanical properties of hybrid fabricated Ti-6.5Al-3.5Mo-1.5Zr-0.3Si titanium alloy by laser additive manufacturing, Mater. Sci. Eng. A 607 (2014) 427–434.

[12] A. Basak, S. Das, Epitaxy and microstructure evolution in metal additive manufacturing, Ann. Rev. Mater. Res. 46 (1) (2016) 125–149.

[13] A. Zinoviev, O. Zinovieva, V. Ploshikhin, V. Romanova, R. Balokhonov, Evolution of grain structure during laser additive manufacturing. Simulation by a cellular automata method, Mater. Des. 106 (2016) 321–329.

[14] H. Helmer, A. Bauereiß, R.F. Singer, C. Körner, Grain structure evolution in Inconel 718 during selective electron beam melting, Mater. Sci. Eng. A 668 (2016) 180–187.

[15] J. Song, Y. Chew, G. Bi, X. Yao, B. Zhang, J. Bai, S.K. Moon, Numerical and experimental study of laser aided additive manufacturing for melt-pool profile and grain orientation analysis, Mater. Des. 137 (2018) 286–297.

[16] J.H. Martin, B.D. Yahata, J.M. Hundley, J.A. Mayer, T.A. Schaedler, T.M. Pollock, 3D printing of high-strength aluminium alloys, Nature 549 (7672) (2017) 365–369.

[17] M. Ma, Z. Wang, X. Zeng, Effect of energy input on microstructural evolution of direct laser fabricated IN718 alloy, Mater. Charact. 106 (2015) 420–427.

[18] G.P. Dinda, A.K. Dasgupta, J. Mazumder, Texture control during laser deposition of nickel-based superalloy, Scr. Mater. 67 (5) (2012) 503–506.

[19] T.M. Rodgers, J.D. Madison, V. Tikare, Simulation of metal additive manufacturing microstructures using kinetic Monte Carlo, Comput. Mater. Sci. 135 (2017) 78–89.

[20] K.L. Johnson, T.M. Rodgers, O.D. Underwood, J.D. Madison, K.R. Ford, S.R. Whetten, D.J. Dagel, J.E. Bishop, Simulation and experimental comparison of the thermo-mechanical history and 3D microstructure evolution of 304L stainless steel tubes manufactured using LENS, Comput. Mech. 61 (5) (2017) 559–574.

[21] O. Zinovieva, A. Zinoviev, V. Ploshikhin, Three-dimensional modeling of the microstructure evolution during metal additive manufacturing, Comput. Mater. Sci. 141 (2018) 207–220.

[22] J.A. Koepf, M.R. Gotterbarm, M. Markl, C. Körner, 3D multi-layer grain structure simulation of powder bed fusion additive manufacturing, Acta Mater. 152 (2018) 119–126.

[23] G.L. Knapp, T. Mukherjee, J.S. Zuback, H.L. Wei, T.A. Palmer, A. De, T. DebRoy, Building blocks for a digital twin of additive manufacturing, Acta Mater. 135 (2017) 390–399.

[24] J. Akram, P. Chalavadi, D. Pal, B. Stucker, Understanding grain evolution in additive manufacturing through modeling, Addit. Manuf. 21 (2018) 255–268.

[25] A. De, T. DebRoy, A smart model to estimate effective thermal conductivity and viscosity in the weld pool, J. Appl. Phys. 95 (9) (2004) 5230–5240.

[26] O. Hunziker, D. Dye, R.C. Reed, On the formation of a centreline grain boundary during fusion welding, Acta Mater. 48 (17) (2000) 4191–4201.

[27] V. Manvatkar, A. De, T. DebRoy, Spatial variation of melt pool geometry, peak temperature and solidification parameters during laser assisted additive manufacturing process, Mater. Sci. Technol. 31 (8) (2015) 924–930.

[28] V. Manvatkar, A. De, T. DebRoy, Heat transfer and material flow during laser assisted multi-layer additive manufacturing, J. Appl. Phys. 116 (12) (2014) Article number: 124905.

[29] T. Mukherjee, H. Wei, A. De, T. DebRoy, Heat and fluid flow in additive manufacturing—part I: modeling of powder bed fusion, Comp. Mater. Sci. 150 (2018) 304–313.

[30] T. Mukherjee, V. Manvatkar, A. De, T. DebRoy, Dimensionless numbers in additive manufacturing, J. Appl. Phys. 121 (6) (2017).

[31] K. Mills, Recommended Values of Thermophysical Properties for Selected Commercial Alloys, Woodhead Publishing Limited, England, 2002.

[32] T. Mukherjee, H.L. Wei, A. De, T. DebRoy, Heat and fluid flow in additive manufacturing - part II: powder bed fusion of stainless steel, and titanium, nickel and aluminum base alloys, Comp. Mater. Sci. (2018).

[33] S. Mishra, T.J. Lienert, M.Q. Johnson, T. DebRoy, An experimental and theoretical study of gas tungsten arc welding of stainless steel plates with different sulfur concentrations, Acta Mater. 56 (9) (2008) 2133–2146.

[34] Y.S. Lee, M. Nordin, S.S. Babu, D.F. Farson, Influence of Fluid Convection on Weld Pool formation in laser cladding, Weld. J. 93 (8) (2014) 292s–300s.

[35] T. Mukherjee, W. Zhang, T. DebRoy, An improved prediction of residual stresses and distortion in additive manufacturing, Comput. Mater. Sci. 126 (2017) 360–372.

[36] T. Mukherjee, J.S. Zuback, W. Zhang, T. DebRoy, Residual stresses and distortion in additively manufactured compositionally graded and dissimilar joints, Comp. Mater. Sci. 143 (2018) 325–337.

[37] S. Mishra, T. DebRoy, Grain topology in Ti–6Al–4V welds—Monte Carlo simulation and experiments, J. Phys. D Appl. Phys. 37 (15) (2004) 2191–2196.

[38] L. Zhang, A.D. Rollett, T. Bartel, D. Wu, M.T. Lusk, A calibrated Monte Carlo approach to quantify the impacts of misorientation and different driving forces on texture development, Acta Mater. 60 (3) (2012) 1201–1210.

[39] Z. Yang, J.W. Elmer, J. Wong, T. DebRoy, Evolution of titanium arc weldment macro and microstructures - Modeling and real time mapping of phases, Weld. J. 79 (4) (2000) 97s–112s.

[40] J.H. Gao, R.G. Thompson, Real time-temperature models for Monte Carlo

simulations of normal grain growth, Acta Mater. 44 (11) (1996) 4565–4570.

[41] B. Radhakrishnan, T. Zacharia, Simulation of curvature-driven grain growth by using a modified Monte Carlo algorithm, Metall. Mater. Trans. A 26 (1) (1995) 167–180.

[42] R.B. Potts, Some generalized order-disorder transformations, Proc. Camb. Philos. Soc. 48 (1) (1952) 106–109.

[43] Z. Jian, K. Kuribayashi, W. Jie, Solid-liquid interface energy of metals at melting point and undercooled state, Mater. Trans. 43 (4) (2002) 721–726.

[44] K.I. Hirano, R. Agarwala, B. Averbach, M. Cohen, Diffusion in cobalt-nickel alloys, J. Appl. Phys. 33 (10) (1962) 3049–3054.

[45] D. Prokoshkina, V.A. Esin, G. Wilde, S.V. Divinski, Grain boundary width, energy and self-diffusion in nickel: effect of material purity, Acta Mater. 61 (14) (2013) 5188–5197.

[46] P. Sahoo, T. Debroy, M.J. McNallan, Surface-tension of binary metal-surface-active solute systems under conditions relevant to welding metallurgy, Metall. Trans. B 19 (3) (1988) 483–491.

[47] H.L. Wei, S. Pal, V. Manvatkar, T.J. Lienert, T. DebRoy, Asymmetry in steel welds with dissimilar amounts of sulfur, Scr. Mater. 108 (2015) 88–91.

[48] Z. Gan, G. Yu, X. He, S. Li, Surface-active element transport and its effect on liquid metal flow in laser-assisted additive manufacturing, Int. Commun. Heat Mass Transf. 86 (2017) 206–214.

[49] Z. Gan, G. Yu, X. He, S. Li, Numerical simulation of thermal behavior and multi-component mass transfer in direct laser deposition of Co-base alloy on steel, Int. J.

Heat Mass Transf. 104 (2017) 28–38.

[50] H.L. Wei, J.W. Elmer, T. DebRoy, Origin of grain orientation during solidification of an aluminum alloy, Acta Mater. 115 (2016) 123–131.

[51] N. Raghavan, R. Dehoff, S. Pannala, S. Simunovic, M. Kirka, J. Turner, N. Carlson, S.S. Babu, Numerical modeling of heat-transfer and the influence of process parameters on tailoring the grain morphology of IN718 in electron beam additive manufacturing, Acta Mater. 112 (2016) 303–314.

[52] Y.S. Lee, W. Zhang, Modeling of heat transfer, fluid flow and solidification microstructure of nickel-base superalloy fabricated by laser powder bed fusion, Addit. Manuf. 12 (2016) 178–188.

[53] Y.M. Ren, X. Lin, X. Fu, H. Tan, J. Chen, W.D. Huang, Microstructure and deformation behavior of Ti-6Al-4V alloy by high-power laser solid forming, Acta Mater. 132 (2017) 82–95.

[54] S. Kou, Welding Metallurgy, 2nd ed., John Wiley & Sons, Hoboken, NJ, 2003.

[55] P.D. Lee, P.N. Quested, M. McLean, Modelling of Marangoni effects in electron beam melting, Philos. Trans. Math. Phys. Eng. Sci. 356 (1739) (1998) 1027–1043.

[56] M.J. McNallan, T. Debroy, Effect of temperature and composition on surface-tension in Fe-Ni-Cr alloys containing sulfur, Metall. Trans. B 22 (4) (1991) 557–560.

[57] Y.S. Lee, D.F. Farson, Surface tension-powered build dimension control in laser additive manufacturing process, Int. J. Adv. Manuf. Technol. 85 (5-8) (2016) 1035–1044.

[58] J.J. Blecher, T.A. Palmer, T. DebRoy, Solidification map of a nickel-base alloy, Metall. Mater. Trans. A 45 (4) (2014) 2142–2151.